International Journal of Nanomedicine

Dovepress
Taylor & Francis Group

Open Access Full Text Article

ORIGINAL RESEARCH

Lipid-Coated Ag@MnO_2 Core-Shell Nanoparticles for Co-Delivery of Survivin siRNA in Breast Tumor Therapy

Jing Zhang[1,2], Min Zha[1], Shanghua Xiao[1], Nina Filipczak[3], Satya Siva Kishan Yalamarty[4], Xiangping Wu[1], Chenkai Gong[1], Xiang Li[1]

[1]Key Laboratory of Modern Preparation of TCM, Ministry of Education, National Key Laboratory for the Modernization of Classical and Famous Prescriptions of Chinese Medicine, National Pharmaceutical Engineering Center for Solid Preparation in Chinese Herbal Medicine, Jiangxi University of Chinese Medicine, Nanchang, Jiangxi, 330004, People's Republic of China; [2]Jiangzhong Pharmaceutical Co. Ltd, Nanchang, Jiangxi, 330049, People's Republic of China; [3]Center for Pharmaceutical Biotechnology and Nanomedicine, Northeastern University, Boston, MA, 02115, USA; [4]Department of Biomedical Engineering, Tufts University, Medford, MA, 02155, USA

Correspondence: Xiang Li, Key Laboratory of Modern Preparation of TCM, Ministry of Education, National Key Laboratory for the Modernization of Classical and Famous Prescriptions of Chinese Medicine, National Pharmaceutical Engineering Center for Solid Preparation in Chinese Herbal Medicine, Jiangxi University of Chinese Medicine, Meiling Road 1688, Xinjian District, Nanchang, Jiangxi, 330004, People's Republic of China, Tel/Fax +86 79187119661, Email xiang.li@jxutcm.edu.cn

Objective: Nanoparticles constructed with silver/manganese dioxide (Ag@MnO_2) as the core, in conjunction with survivin siRNA (sis) and cyclo(RGD-DPhe-K) (Ag@MnO_2-sis-c-L), were prepared for integrated tumor diagnosis and therapy.

Methods: Ag@MnO_2-sis-c-L particles were prepared and characterized. The silver and manganese content were determined by inductively coupled plasma optical emission spectroscopy (ICP-OES). The stability of sis in the system was evaluated by incubation with 50% FBS before the agarose gel electrophoresis experiment. The in vitro photothermal conversion ability, cytotoxicity to 4T1 cells, and cellular uptake of preparations were evaluated. The dialysis technique was employed to determine the in vitro release profile of Ag and Mn from Ag@MnO_2-sis-c-L under various pH conditions. The pharmacokinetic behavior and tissue distribution of silver in vivo were detected by ICP-OES. Animal model experiments were conducted to further evaluate the anti-tumor efficacy of Ag@MnO_2-sis-c-L against breast cancer in combination with infrared irradiation.

Results: Our newly synthesized Ag@MnO_2-sis-c-L nanoparticles displayed superior physicochemical properties. The combined application of these nanoparticles with photothermal therapy (PTT) exerted the strongest synergistic inhibitory effects on tumor growth. Survivin protein expression in tumor tissues were markedly suppressed following delivery of nanoparticles loaded with sis. Additionally, magnetic resonance imaging revealed the high imaging capability of hybrid nanoparticles.

Conclusion: This study supports the potential utility of Ag@MnO_2-sis-c-L coupled with PTT in therapeutic and diagnostic imaging applications.

Keywords: survivin siRNA, breast cancer, photothermal therapy, Ag@MnO_2, combination therapy

Introduction

Breast cancer (BC) is a major health concern worldwide, owing to its high incidence and mortality rates. The global incidence of breast cancer is projected to reach 440 million cases by 2070.[1,2] In China, the annual incidence of breast cancer continues to increase, with an estimated 420,000 new cases per year, ranking first in terms of the prevalence of female cancers.[3] However, traditional cancer treatment methods, including radiotherapy, chemotherapy, and surgery, have several limitations, such as a high surgical risk and significant physical injury, which restrict their further application and development.[4] Targeted drug therapy has the advantages of fewer side effects and higher therapeutic efficacy.[5] The synergistic integration of targeted therapeutic agents with multimodal treatment strategies represents a critical direction for breast cancer management.

Received: 5 December 2024
Accepted: 12 May 2025
Published: 22 May 2025

Photothermal therapy (PTT) is an innovative treatment method that uses a specific light source to irradiate and increase the temperature to achieve therapeutic purposes; it not only has the advantages of light source penetration and controllable area of illumination, but also significantly reduces the adverse effects of conventional therapy.[6–8] The multiple functions of MnO_2 have also been reported. MnO_2 exhibits both photothermal and magnetic properties.[9,10] Due to the potent magnetic properties of Mn^{2+}, the particles can be visualized under MRI, which presents a valuable tool for tumor diagnosis.[11] In addition, MnO_2 has been characterized as a loose mesoporous material with a large specific surface area that has a strong loading capacity for metal nanoparticles.[12] Therefore, based on our previous work,[13,14] we designed to hybrid the MnO_2 nanoparticles with nanosilver, which is an exceptional type of nanomaterial with unique physico-chemical properties, including strong interactions between particles,[15] antimicrobial activity,[16] and anti-tumor activity.[17] Therefore, we assumed that the combined application of the two metal nanoparticles could not only exert the anti-tumor effect of nanosilver but also enhance the overall photothermal and diagnostic effects of MnO_2 in the tumor microenvironment. The effectiveness of this combined application in cancer therapy has not been documented to date.

However, premature release and accumulation of nanosilver in vivo can trigger potential toxicity.[13] It was reported that coating of nanosilver with polymer-carriers could minimize its toxicity while still exerting excellent antibacterial effects.[18] Thus, the fabrication of composite materials could serve as a viable method for effectively harnessing the potent capabilities of metal particles.

Survivin is a member of the apoptosis-inhibitor family. The overexpression of survivin in breast cancer patients inhibits apoptosis and enhances tumor cell proliferation.[19] Based on the finding that survivin overexpression can be induced by PTT, which leads to the thermoresistance of cancer cells,[20] to maximize the effect of PTT, we seek to investigate the therapeutic efficacy combined with the blockage of survivin protein and PTT. Small interfering RNA (siRNA) therapy, based on post-transcriptional gene silencing, is typically selective and effective. Accordingly, the inhibition of survivin overexpression at the tumor site using gene therapy with sis is considered a potential therapeutic option. Since nucleic acids are susceptible to degradation by nucleases, the selection of an appropriate carrier for delivery is crucial for enhancing the stability of siRNAs.[21]

Therefore, in this study, we synthesized nanoparticles comprising nanosilver loaded on MnO_2 as the core, encapsulated with synthetic phospholipid to load siRNA, and modified the surface of the nanoparticles with cRGD. On the one hand, the positively charged lipid material effectively binds negatively charged nucleic acid molecules through electrostatic adsorption, and on the other, cRGD modification on the surface of the preparation not only addresses the challenge of siRNA cellular entry and low stability but also specifically inhibits the expression of abnormal integrin $\alpha_v\beta_3$ at the tumor site.[22] The novel formulation achieved long-circulating targeted delivery and synergistic anti-tumor effects. The cytotoxicity and cellular uptake capability of the formulation were comprehensively evaluated, along with its anti-cancer efficacy in vivo.

Materials and Methods

Materials

Survivin siRNA (5′-GAACAUCAUCAUCCAGGAC-3′) was purchased from Ribo Biotechnology Co., Ltd., Guangzhou, China. 1,2-Dipalmitoyl-sn-glycero-3-phosphoethanolamine-N-(polyethylene glycol)-2000-cRGD (DSPE-PEG2000-cRGD) was obtained from Xi'an Ruixi Biotechnology Co., Ltd., Xi'an, China. SM-102, hydrogenated soy phosphatidylcholine (HSPC), 1,2-dimyristoyl-rac-glycero-3-methoxypolyethylene glycol-2000 (DMG-PEG2000), and cholesterol-high purity (CHO-HP) were purchased from AVT (Shanghai) Pharmaceutical Tech Co., Ltd. (Shanghai, China). Silver nitrate was obtained from Aladdin Biochemical Technology Co. Ltd. (Shanghai, China). Poly (allylamine hydrochloride) (PAH) from Shanghai Aladdin Biochemical Technology Co., Ltd. The H&E staining kit was purchased from Beijing Solarbio Science and Technology Co., Ltd. (Beijing, China). The liver and kidney index measurement kits were obtained from Beijing Leadman Biochemistry Co., Ltd. (Beijing, China). All reagents were chromatographically and analytically pure.

Cells

Murine breast cancer 4T1 cells and fibroblast L929 cells were purchased from Beijing Dingguo Changsheng Biotechnology Co., Ltd. and cultured in Roswell Park Memorial Institute (RPMI) 1640 medium and Dulbecco's Modified Eagle Medium (DMEM), respectively, containing 10% (v/v) fetal bovine serum (FBS) and 1% PS (Solarbio) in an incubator at 37°C with 5% CO_2.

Animals

Female BALB/c mice (18–20 g) and female Sprague-Dawley rats (200 ± 20 g) were provided by SPF (Beijing) Biotechnology Co., Ltd. (Certificate No SCXK (Jing) 2019–0010). Animal experiments were conducted according to ethical policies and procedures approved by the Medical Ethics Committee of Jiangxi University of Chinese Medicine, Jiangxi, China. Throughout the experimental period, the animal room was well-ventilated and maintained under a regular 12-hour light-dark cycle. The experimental protocols involving animal handling and welfare were sanctioned by the Laboratory Animal Ethics Committee of Jiangxi University of Chinese Medicine, with the approval number JZLLSC20250503.

Preparation of Ag@MnO_2-Sis-c-L Nanoparticles

$AgNO_3$ (0.04 M) and $KMnO_4$ (0.02 M) solutions were prepared, mixed, and added dropwise to 0.3 M PAH solution (volume ratio, 8:1). The mixture was incubated in an ice bath at 900 rpm for 15 min. PAH reduces silver nitrate ($AgNO_3$) and potassium permanganate ($KMnO_4$) to form nanoscale silver and MnO_2 through a chemical reduction reaction. Unreacted materials were removed via dialysis for 4 h using a 20 kDa dialysis membrane. The solution obtained was mixed with 0.1 M citric acid solution before the addition of sis solution. SM-102, CHO-HP, HSPC, and DMG-PEG2000 were mixed with anhydrous ethanol at a molar ratio of 18:16:4:1. The ethanolic lipid solution was injected into the Ag@MnO_2 solution at a temperature of 55°C and rotation speed of 600 rpm for 30 min. The resulting system was dialyzed for 4 h in a 20 kDa dialysis bag to obtain Ag@MnO_2-sis-L.

Following the same reaction conditions and steps, a preheated ethanolic solution of phospholipid SM-102, CHO-HP, HSPC, DMG-PEG2000, and DSPE-PEG2000-cRGD at a molar ratio of 18:16:4:0.9:0.1 was added and injected into the Ag@MnO_2 solution, resulting in the formation of Ag@MnO_2-sis-c-L.

Agarose Gel Electrophoresis

The efficiency of siRNA encapsulation by Ag@MnO_2-sis-c-L was determined using agarose gel electrophoresis. The Ag@MnO_2 core was prepared and mixed with 10 μL of 20 μmol/L siRNA and phospholipids at different concentrations. Mixtures were vortexed for 3 min and incubated at 37°C for 30 min to prepare samples with variable N:P ratios (10:1, 5:1, 1:1, 1:5, 1:10, and 1:20) calculated using SM-102. An appropriate volume of the sample was loaded into the wells of an agarose gel (E-Gel 1.2% with SYBR Safe, Invitrogen, Thermo Fisher Scientific), and electrophoresis was performed at a constant voltage of 65V applied for 30 min (E-Gel Power Snap Electrophoresis Device, Invitrogen, Thermo Fisher Scientific). A gel imaging system (E-Gel Power Snap Camera, Invitrogen, Thermo Fisher Scientific) was used to obtain gel images.

Size and Morphological Analyses

The size, PDI, and zeta potential of nanoparticles were measured using a Malvern particle size analyzer (ZEN3690, Malvern, UK). The nanoparticles were diluted to an appropriate volume with ultrapure water at 25°C prior to analysis. The morphology of the nanoparticles was characterized by field-emission scanning electron microscopy (SEM) (SU8010, Hitachi Ltd., Tokyo, Japan) and transmission electron microscopy (TEM) (JEM-2100, JEOL, Tokyo, Japan).

Surface Elemental Analysis

Experiments were performed using a SU8010 SEM operated at a 10 kV accelerating voltage. The spatial resolution of the microscope is approximately 1.3 nm. A Bruker Flash6I60 Energy-Dispersive Spectrometer (EDS) was used to determine the composition of the formulation.

Ag and Mn Content Determination

Inductively coupled plasma optical emission spectroscopy (ICP-OES) (700ES, Varian, Palo Alto, CA, USA) was pre-conditioned to meet experimental requirements by cooling the cyclone and achieving the desired temperature. The radiofrequency power was set to 1.5 kW, and the flow rate of high-purity Argon gas was adjusted to 1.5 L/min. The nebulizer temperature was maintained at 2.5°C with a flow rate of 0.8 L/min. Following experimental needs, the peristaltic pump speed was set to 15 rpm to regulate the sample intake rate to 1 mL/min. Experiments were conducted in triplicate, and the final sample concentrations were calculated based on intensity values.

Simulated Serum Stability

The Ag@MnO_2-sis-c-L formulation was added to the solution containing 50% FBS at a 1:1 volume ratio. The mixture was vortexed to ensure homogeneity and incubated at 37°C. The reactions were conducted at various time intervals (0, 1, 2, 4, 8, 12, and 24 h). The control group was prepared using free lysis under the same conditions. Following the incubation period, the samples were treated with heparin sodium at a concentration of 10 IU/μg to displace the sis. The mixture was agitated on a shaking platform for 30 minutes at 37°C. An appropriate volume of the sample was loaded into the wells of an agarose gel (E-Gel 1.2% with SYBR Safe, Invitrogen, Thermo Fisher Scientific) and electrophoresis was performed at a constant voltage of 65V applied for 15 min (E-Gel Power Snap Electrophoresis Device, Invitrogen, Thermo Fisher Scientific). A gel imaging system (E-Gel Power Snap Camera, Invitrogen, Thermo Fisher scientific) was used to obtain gel images.

Photothermal Conversion Capability

Using water as a negative control, the photothermal effect of Ag@MnO_2-sis-c-L irradiated at a wavelength of 808 nm and a power density of 2.50 W/cm³ was determined using an infrared temperature probe (TES-1310, Suzhou Runqi Electronic Technology Co., Ltd, Suzhou, China).

Cytotoxicity

The influence of Ag@MnO_2, Ag@MnO_2-sis-L, and Ag@MnO_2-sis-c-L on the viability of 4T1 and L929 cells was investigated using the CCK-8 assay (Beijing Biolaibo Technology Co., Ltd., Shanghai, China). Cells were seeded at a density of 1×10^4 cells per well in 96-well plates and cultured in an incubator at 37°C and 5% CO_2. Cells were treated with different preparations in serum complete media at an Ag concentration of 0.2 μg/mL, and the preparations were removed after 1 to 2 h of incubation, and fresh culture media were added.[23] After 24 h incubation, 10 μL of CCK-8 detection reagents were added to each well. After 2 h of culture, absorbance at 450 nm in each well was measured using a microplate reader (Synergy H1, BioTek, VT, USA). Cell viability in response to the different nanoformulations was calculated.

Cellular Uptake

The 4T1 cells were plated at a density of 2×10^6 cells/well in six-well plates. The Ag@MnO_2-sis-L and Ag@MnO_2-sis-c-L formulations were pre-diluted with the culture medium to a concentration of 5 μg/mL and co-incubated with 4T1 cells for variable durations of 2, 5, 10, and 15-min. Cells were collected at the end of each incubation period, and intracellular Ag content was determined using inductively coupled plasma optical emission spectroscopy (ICP-OES).

In vitro Release

The dialysis technique was utilized to assess the in vitro release profile of Ag@MnO_2-sis-c-L under specific pH conditions that are characteristic of both normal and tumor microenvironments. An aliquot of the Ag@MnO_2-sis-c-L formulation (1 mL) was loaded into a dialysis bag with a molecular weight cutoff of 20 kDa and immersed in 100 mL of 0.5% polysorbate 80 PBS solution adjusted to pH levels of 5.0 and 7.4. The release of Ag and Mn ions was monitored at 37°C at a stirring speed of 100 rpm. At predetermined time points (0.5, 1, 2, 4, 8, 12, and 24 h), samples were collected, and an equal volume of release medium at the same temperature was replenished. The concentrations of Ag and Mn in the release medium were quantified by ICP-OES.

Pharmacokinetics Research

Female Sprague-Dawley (SD) rats with similar body weights (200–220g) were randomly divided into three groups receiving different nanoformulations: Ag@MnO_2, Ag@MnO_2-sis-L, and Ag@MnO_2-sis-c-L. The rats were fasted overnight before the experiment. Each rat was injected with nanoformulations at a dosage of 0.8 mL/kg, equivalent to the Ag content through the tail vein. Following injection, 500 μL blood samples were collected from the ocular sinus at 1 min, 5 min, 15 min, 30 min, 1 h, 2 h, 4 h, 8 h, 12 h, 24 h, and 48 h. Blood samples were digested using an aqua regia solution. The Ag content in samples was analyzed using ICP-OES. Temporal changes in the Ag contents of the three groups of nanoformulations were calculated, and pharmacokinetic parameters, were derived from the data.

Biodistribution

When the tumor volume of 4T1 breast tumor-bearing mice reached 300 mm^3, the Ag@MnO_2-sis-L and Ag@MnO_2-sis-c-L formulations were administered via tail vein injection. At time points of 0.5 h, 4 h, and 12 h post-injection, the mice were euthanized, and the heart, liver, spleen, lung, kidney, and tumor tissues were extracted. The tissues were rinsed with physiological saline, blotted dry with a filter paper, and weighed. An appropriate amount of tissue was used to prepare a 100 mg/mL tissue homogenate, which was subsequently digested using an aqua regia solution. The Ag contents in the main organs and tumors at different time points were evaluated using ICP-OES.

Anti-Tumor Efficacy

A 4T1 tumor-bearing mouse model of breast cancer was established, and the experiment was conducted at tumor volumes of ~100 mm^3. The mice were randomly divided into nine groups: model, Free sis, Ag@MnO_2-c-L, Ag@MnO_2-sis-c-L, Ag@MnO_2-scrsis-c-L, Free sis-NIR, Ag@MnO_2-c-L-NIR, Ag@MnO_2-scrsis-c-L-NIR, and Ag@MnO_2-sis-c-L-NIR. The animals were administered the formulations via tail vein injection once a week for a total of four times (at a dose of 3.75 mg/kg of Ag equivalent). Two hours after administration, the tumor sites of mice in the photo-irradiation groups were exposed to 2.5 W/cm^3 power at 808 nm infrared irradiation for 5 min. Tumor volumes were calculated as follows:

$$V = \left(D^2 \times L\right)/2$$

where L represents the longest diameter on the tumor surface, D the shortest diameter on the tumor surface, and V the tumor volume.

Western Blot Analysis

After the experimental period, 100 mg of tumor tissue from each group was incubated in precooled RIPA lysis buffer (protease inhibitors were added at a ratio of 1:100 before use). The tissue was homogenized on ice and placed on a shaker at 4°C for 2 h, followed by centrifugation at 1000 g for 10 min at 4°C. The protein-containing supernatant fraction was collected, and the protein concentrations of each group was determined using a BCA assay kit (CW0014S, Jiangsu Cowin Biotech Co., Ltd, Jiangsu, China). Protein samples (40 μg) were electrophoretically separated using a NuPAGE 4−12% Bis-Tris SDS-PAGE gel and transferred to a polyvinylidene fluoride membrane (PVDF, Thermo Scientific, MA, USA). PVDF membranes were blocked with 5% BSA in PBS Tween 20 (Fisher Scientific, Fair Lawn, NJ, USA) for 1 h and incubated overnight at 4°C with primary antibodies (1:1000 dilution; survivin and β-actin, Abcam), followed by incubation with horseradish peroxidase-conjugated secondary anti-rabbit IgG antibody (1:1000 dilution; Cell Signal Technology, Danvers, MA, USA) for 1 h at room temperature. The membranes were washed and visualized with a ChemiDoc XRS+ imaging system (Bio-Rad, Hercules, CA, USA) using β-actin as the loading control. ImageJ software (National Institutes of Health) was used for the semi-quantitative measurement of the mean gray value normalized to β-actin expression.

In vivo Photothermal Conversion

Ag@MnO_2-sis-c-L (Ag equivalents of 37.5 and 75.0 μg/mL) was administered to mice via tail vein injection. After 2 h, mice in each group were anesthetized, and tumor tissue was irradiated at 808 nm laser wavelength with the power density

of 2.5 W/cm^3 for 80s. A temperature probe was used to measure the body temperature in each group using an infrared thermal imager (Testo 865, Testo AG, Schwarzwald, Germany), particularly at the tumor site, to determine the photothermal conversion efficiency of the formulation at the tumor location.

Magnetic Resonance Imaging

The mice were administered the Ag@MnO_2-sis-c-L formulation (Ag equivalent of 3.75 mg/kg) via tail vein injection. Immediately afterward, the mice were positioned within the MRI apparatus (SKYSCAN1276, Bruker Corporation, DEU) to expose the tumor region and subjected to comprehensive MRI scanning. MRI images were captured at intervals of 0.167, 0.5, 1, 2, and 3 h post-injection to evaluate contrast enhancement effects at the tumor location.

Mouse Weight Monitoring

The physiological toxicity of the formulation in mice was evaluated by monitoring daily fluctuations in body weight, along with the general health and vigor of the animals.

Assessment of Biochemical Parameters

At the end of the experimental period, 400 μL aliquots of blood samples were collected from the orbital venous plexus of mice, centrifuged at 4°C for 10 min, and the supernatant fractions were used for analysis. Blood biochemical parameters from mice in each group were assessed using a fully automatic biochemical analyzer (7100; Hitachi, Ltd., Tokyo, Japan) with specific reagent kits for mouse liver and kidney function indicators, including alanine aminotransferase (ALT), aspartate aminotransferase (AST), blood urea nitrogen (BUN), and creatinine (CRE-L).

H&E Staining

At the end of the anti-tumor efficacy experimental period, the heart, liver, spleen, lung, kidney, and tumor tissues were collected, fixed in polyformaldehyde solution for 24 h, and rinsed for 12 h. Subsequently, tissues were dehydrated using a biological tissue dehydrator under the following gradient elution process: 70%, 85%, and 95% ethanol for 1 h each, followed by two rounds of 100% ethanol dehydration for 30 min each. Tissues were subsequently cleared with xylene for 20 min and infiltrated with paraffin for 2 h. Next, the tissues were embedded, and paraffin sections were generated using a microtome. Sections were stained using the H&E staining procedure. The sections were initially deparaffinized by soaking in xylene, gradient-eluted with a series of ethanol concentrations, washed with distilled water, and stained using a hematoxylin-eosin kit. A neutral resin was applied for the coverslip treatment. Stained tissue sections were observed under a light microscope.

Statistical Analysis

Results are expressed as the mean ± standard deviation (SD). Statistical analysis was conducted using one-way analysis of variance and Student's *t*-test using the SPSS software (version 20.0). Statistical significance was set at $p < 0.05$.

Results and Discussion

Preparation and Characterization of Nanoparticles

Agarose gel electrophoresis revealed a correlation between the N:P ratio (the ratio between the amine groups of the ionizable lipid (N) and phosphate groups of the cargo (P)) and the encapsulation efficiency of siRNA in Ag@MnO_2-sis-c-L using free siRNA as a control. Complete encapsulation of siRNA was achieved at N:P ratios ≥5, resulting in the selection of 5:1 as the optimal ratio (Figure 1A). The particle diameter values of Ag@MnO_2, Ag@MnO_2-sis-L, and Ag@MnO_2-sis-c-L were less than 100nm, with PDIs lower than 0.3 (Table 1). Because the N:P ratio was 5:1, positive zeta potentials were achieved due to the extra positive charge of SM-102. Scanning electron microscopy (SEM) results indicated that all three nanoparticles exhibited good dispersibility (Figure 1B). Transmission electron microscopy (TEM) revealed the spherical or elliptical morphology of nanoparticles (Figure 1C). In chemical reduction reactions, the choice of reducing agent determines the morphology and performance of the metal nanoparticles. Sodium borohydride,

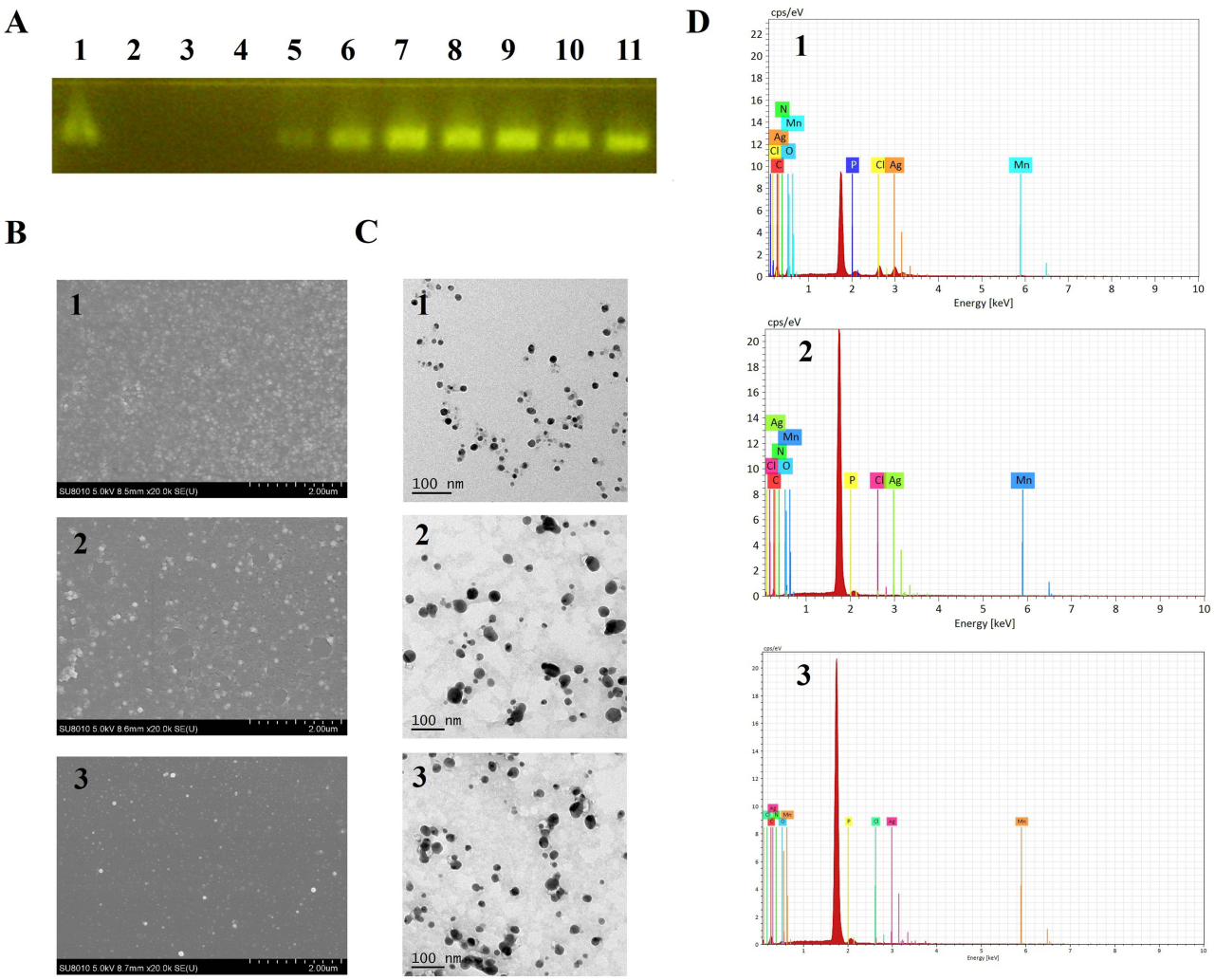

Figure 1 (**A**) Agarose gel electrophoresis of Ag@MnO_2-sis-c-L to siRNA (Lane 1: Free siRNA; Lane 2: Ag@MnO_2-c-L; Lanes 3–11: Ag@MnO_2-sis-c-L N:P 10:1; 5:1; 1:1; 1:5; 1:10; 1:20; 1:40; 1:80; 1:160); (**B**) SEM and (**C**) TEM images of Ag@MnO_2 (1), Ag@MnO_2-sis-L (2), and Ag@MnO_2-sis-c-L (3); (**D**) Surface element maps of Ag@MnO_2 (1), Ag@MnO_2-sis-L (2), and Ag@MnO_2-sis-c-L (3).

a commonly used reducing agent, can rapidly nucleate to form metal nanoparticles, as previously reported.[24,25] However, the use of a strong reducing agent leads to excessively fast reaction rates, making it difficult to control the morphology of metal nanoparticles and prone to aggregation. In this study, the Ag@MnO_2 core nanoparticles obtained by mild reduction with PAH have smaller diameters, clear morphologies, and high metal element content.[26] In addition, after the phospholipid's encapsulation, the zeta potential of the nanoparticles changed from negative to positive. This phenomenon can be attributed to the use of the SM-102. The ionizable cationic lipid SM-102 becomes protonated and positively charged under acidic conditions, allowing it to bind to negatively charged siRNA through electrostatic interactions and form stable lipoplexes. SM-102 is commonly used in nanoparticles for nuclear acid delivery to protect mRNA molecules from degradation by enzymes in the body and to promote their effective entry into human cells.[27] However, nanoparticles with strong positive charges are easily recognized and eliminated by the immune system in the bloodstream.[28] DMG-PEG2000[29,30] and DSPE-PEG2000-cRGD[31] were included in the formula to provide PEG shield for long circulation and targeting effect and as a result the zeta potentials of Ag@MnO_2-sis-L and Ag@MnO_2-sis-c-L nanoparticles are 6.54 ± 0.19 and 4.73 ± 0.07, respectively.

Based on the surface elemental analysis, in addition to C, N, O, and Cl elements which are the contribution of PAH, the Ag and Mn elements in Ag@MnO_2 accounted for 49.08% of the overall mass of the formulation (Figure 1D). In contrast, for the Ag@MnO_2-sis-L and Ag@MnO_2-sis-c-L formulations, the contents of Ag and Mn differed: for Ag@MnO_2-sis-L, Ag accounted

https://doi.org/10.2147/IJN.S510514

Table 1 Size, PDI, and Zeta Potential of Nanoparticles

Formulation	Particle Size (nm)	Zeta Potential (mV)	PDI
$Ag@MnO_2$	65.44 ± 1.27	−45.57 ± 1.07	0.089 ± 0.02
$Ag@MnO_2$-sis-L	80.73 ± 0.83	6.54 ± 0.19	0.247 ± 0.01
$Ag@MnO_2$-sis-c-L	84.40 ± 0.20	4.73 ± 0.07	0.234 ± 0.02

Abbreviation: PDI, polydispersity index.

for 5.12% and Mn accounted for 7.85% of the total mass, while for $Ag@MnO_2$-sis-c-L, Ag and Mn composed 0.96% and 5.17% of the total mass, respectively. The elements C, O, N, and P from lipids were predominantly represented, with percentages of 51.68%, 16.46%, 4.03%, and 14.42% ($Ag@MnO_2$-sis-L) and 54.41%, 20.02%, 7.33%, and 12% ($Ag@MnO_2$-sis-c-L), respectively. The increase in the content of C, N, O, and P elements, along with the decrease in the content of Ag and Mn, showed that $Ag@MnO_2$ nanoparticles were effectively encapsulated with lipids.

Ag and Mn contents in the solution were further examined by ICP-OES. The Ag contents in $Ag@MnO_2$-sis-L and $Ag@MnO_2$-sis-c-L were determined as 612.8 ± 1.60 μg/mL and 607.5 ± 3.12 μg/mL, and Mn contents as 257.3 ± 1.61 μg/mL and 245.2 ± 1.31 μg/mL, respectively. Surface modification of DSPE-PEG2000-cRGD had no significant effect on the metal nano-core cargo-loading ability.

Simulated Serum Stability

Images obtained from gel electrophoresis of free sis and $Ag@MnO_2$-sis-c-L incubated with simulated serum at different time points revealed a free sis band after 4 h that completely disappeared after 8 h, indicating that siRNA is not stable over time and undergoes degradation (Figure 2A). However, the sis band in $Ag@MnO_2$-sis-c-L was maintained for a minimum of 12 h, suggesting that the degradation rate of sis in serum was inhibited to some extent, thereby enhancing the stability of sis. Additionally, pharmacokinetic data (Table 2) indicate that $Ag@MnO_2$-sis-c-L nanoparticles have a larger mean residence time (MRT_{0-t}) value compared to $Ag@MnO_2$ nanoparticles.

Photothermal Conversion Efficiency

The photothermal effect of $Ag@MnO_2$-sis-c-L is shown in Figure 2B. The blank control group with distilled water showed a minimal increase in temperature to 27.8°C after 10 min of infrared irradiation, whereas the $Ag@MnO_2$-sis-c-L formulation reached 53°C within 5 min, further increasing to 63.2°C within 10 min. Based on these findings, we inferred that the formulation could rapidly achieve an elevated temperature of over 45°C[32] within a short period, thereby causing hyperthermia and thermolytic death of tumor cells in the body. The photothermal conversion efficiency of $Ag@MnO_2$-sis-c-L remained unchanged after repeated irradiation cycles, indicating that the high photothermal conversion efficiency of the nanoparticles remained unchanged (Figure 2C). PTT typically employs near-infrared (NIR) light and relies on light-absorbing materials to induce localized heating for the treatment of diseases. A key advantage of PTT is the ability to control the position of the light beam exposure, thereby minimizing damage to surrounding healthy tissues, which depends on PPT agents. The $Ag@MnO_2$-sis-c-L nanoparticles could effectively and persistently convert light energy into heat energy, thereby ensuring PPT treatment.

Cytotoxicity

The cytotoxicity effects of $Ag@MnO_2$, $Ag@MnO_2$-sis-L, and $Ag@MnO_2$-sis-c-L against 4T1 and L929 cells were determined using the CCK-8 assay. Under in vitro conditions, prolonged exposure of the target ligand to cells might mitigate its augmented cellular binding effect.[23] Therefore, a relatively short incubation period of 1 and 2 hours led to elevated cytotoxicity in tumoral cells treated with $Ag@MnO_2$-sis-c-L when compared to those treated in L929 cells, as observed 24 hours after treatment (Figure 2D). The modification of cRGD on the surface of $Ag@MnO_2$-sis-c-L promoted cellular binding, thereby contributing to increased cytotoxicity in 4T1 cells. However, nanoparticles also possess inherent toxicity to normal cells, given that in vitro experiments conduct direct exposure of cells to the formulation. The observed

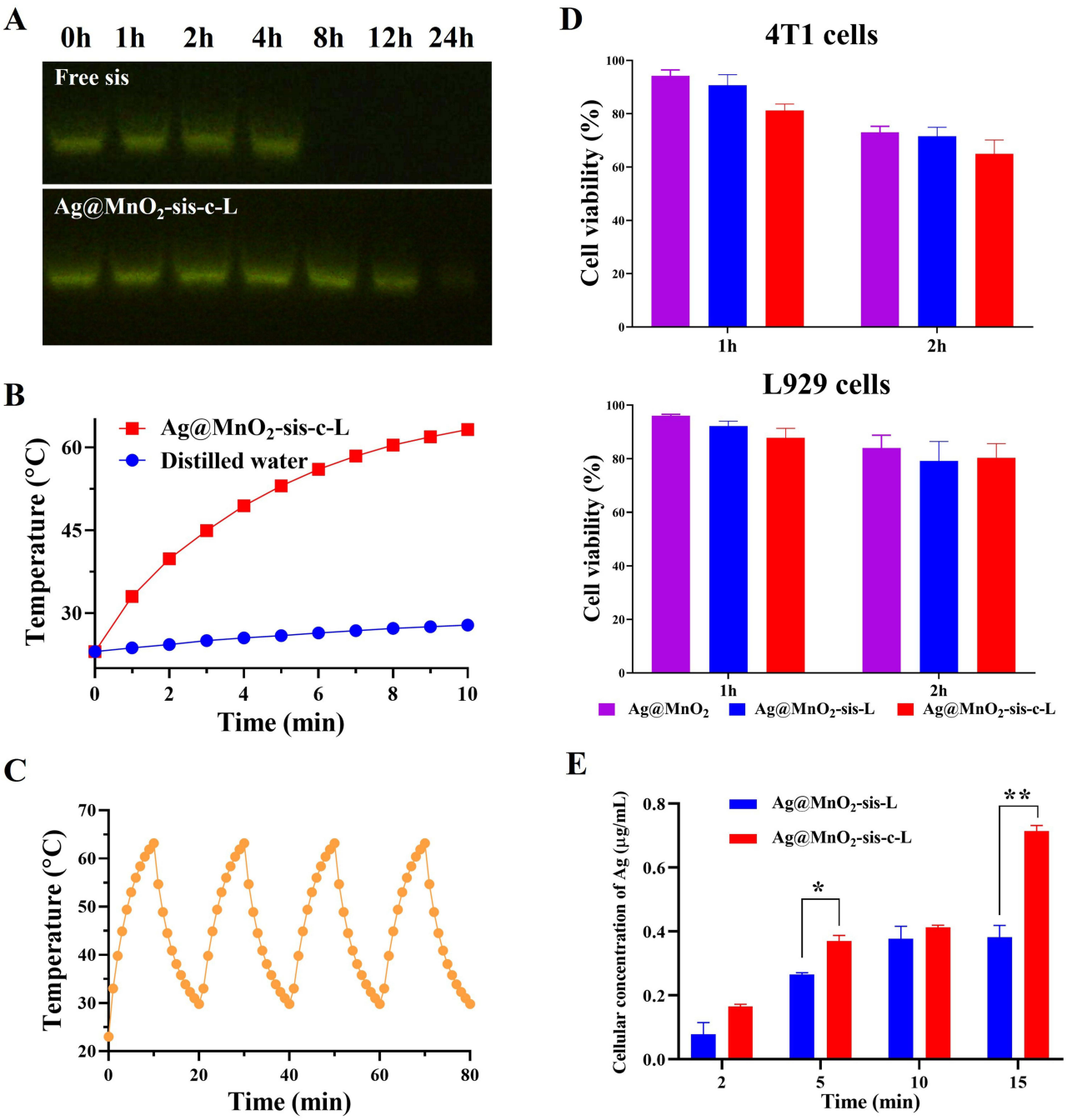

Figure 2 (**A**) Agarose gel electrophoresis of Free sis and Ag@MnO_2-sis-c-L after incubation with simulated serum at different time-points; (**B**) Temperature changes of Ag@MnO_2-sis-c-L under NIR radiation; (**C**) The photothermal conversion efficiency of Ag@MnO_2-sis-c-L after repeated irradiation cycles; (**D**) Cytotoxicity of different preparations containing a 0.2 μg/mL of Ag in 4T1 and L929 cells; (**E**) Cellular uptake of Ag by 4T1 cells treated with Ag@MnO_2-sis-L and Ag@MnO_2-sis-c-L formulations (vs model group, *P<0.05, **P<0.01).

cytotoxicity results further underscore the necessity of developing targeted formulations for in vivo applications, thereby reducing off-target effects and potential harm to healthy tissues.

Cellular Uptake

Ag@MnO_2-sis-L and Ag@MnO_2-sis-c-L were co-cultured with 4T1 cells for various durations (Figure 2E). Compared to Ag@MnO_2-sis-L, Ag@MnO_2-sis-c-L nanoparticles exhibit higher cellular uptake of Ag at all scheduled time points within 15 min. Notably, a significant difference (P<0.05) between the two formulations was observed at the 5-minute

https://doi.org/10.2147/IJN.S510514

Table 2 Pharmacokinetic Parameters of the Nanopreparation Treatment Groups

Analytes	T_{max} (min)	C_{max} (μg/mL ħ)	AUC_{0-t} (μg/mL ħ)	MRT_{0-t}(h)	CL (mg)/(μg/mL)/h	V (mg)/(μg/mL)
Ag@MnO_2	1	3.64 ± 0.18	20.05 ± 0.91	15.1 ± 0.85	0.0066 ± 0.0001	0.18 ± 0.008
Ag@MnO_2-sis-L	1	3.75 ± 0.12	27.05 ± 0.49	16.7 ± 0.68	0.0040 ± 0.0001	0.15 ± 0.002
Ag@MnO_2-sis-c-L	1	4.69 ± 0.06	31.45 ± 1.13	17.6 ± 0.41	0.0030 ± 0.0001	0.15 ± 0.047

Abbreviations: T_{max}, time to the peak plasma concentration; C_{max}, the peak plasma concentrations; AUC: the area under the curve; MRT, mean residence time; CL, clearance; V, the apparent volume of distribution.

mark. At the 15-minute mark, an even more pronounced difference between the two formulations was observed. Additionally, within the 5-minute interval from 10 to 15 min, there was almost no increase in the Ag uptake content in the Ag@MnO_2-sis-L nanoparticle group, whereas a significant increase in Ag uptake content was observed in the Ag@MnO_2-sis-c-L nanoparticle group. These results indicate that surface modification with cRGD further promotes the cellular uptake of nanoparticles.

In vitro Release

The cumulative release profiles of Ag@MnO_2-sis-c-L in PBS containing 0.5% polysorbate 80 at different pH values are presented in Figure 3A. No significant burst release of Ag@MnO_2-sis-c-L was observed over these two pH conditions. At pH 5.0 and 7.4, the cumulative release rates of Ag were 3.06% and 2.17%, and those of Mn were 58.79% and 19.17%, respectively. At a tumor tissue pH of 5.0, the release rates of Ag@MnO_2-sis-c-L were increased relative to those at pH 7.4. The normal physiological pH of the human body ranges from 7.35 to 7.45,[33] whereas the pH of the tumor microenvironment is generally lower than that of normal tissue,[34] typically acidic. This slightly acidic environment is widely present in various types of tumors and plays an important role in the occurrence and development of cancer. Ideally, compared to normal tissues, nanoparticles should release more drugs at the tumor site; in this study, the nanoparticles met these criteria. Figure 3A shows the release profile of the Ag@MnO_2-sis-c-L nanoparticles corresponds to the pH change.

Pharmacokinetic Data

As shown in Table 2 and Figure 3B, the peak plasma concentrations (C_{max}) of Ag@MnO_2-sis-L and Ag@MnO_2-sis-c-L were 1.03 and 1.28 times higher than that of Ag@MnO_2, respectively, indicating that encapsulation of the core is beneficial for the retention of the drug in the bloodstream. Compared to Ag@MnO_2, the area under the curve (AUC_{0-t}) of Ag@MnO_2-sis-L and Ag@MnO_2-sis-c-L groups were 1.34 and 1.57 times higher, respectively, with extended drug retention time and reduced apparent volume of distribution (V). Moreover, relative to Ag@MnO_2, the drug clearance rates of Ag@MnO_2-sis-L and Ag@MnO_2-sis-c-L were reduced by 30% and 45%, respectively. This finding suggests that the hybrid core of Ag@MnO_2 is rapidly cleared, but after encapsulation with lipids, as in the case of Ag@MnO_2-sis-L and Ag@MnO_2-sis-c-L, the drugs are retained for a longer period in the body, with a stronger effect observed for Ag@MnO_2-sis-c-L, which is conducive to enhancing therapeutic efficacy. This result may be due to the highly positive charge of Ag@MnO_2, which serves as a distinct marker for immune recognition once the nanoparticles enter the bloodstream. In contrast, encapsulating the nanoparticles with PEG-conjugated lipids not only reduces their surface charge but also creates steric hindrance, making them less detectable by the complement system.[35] Without such modifications, complement proteins tag nanoparticles for opsonization, leading to rapid clearance by macrophages in the liver and spleen. Additionally, complement activation can contribute to protein corona formation and trigger inflammatory responses.[36] Moreover, the larger size of the Ag@MnO_2-sis-c-L nanoparticles decreased their clearance and enhanced their residence time. A longer residence time is vital in cases where drug exposure can be enhanced while the treatment frequency can be reduced. To further validate the properties of these nanoparticles, a biodistribution study was conducted.

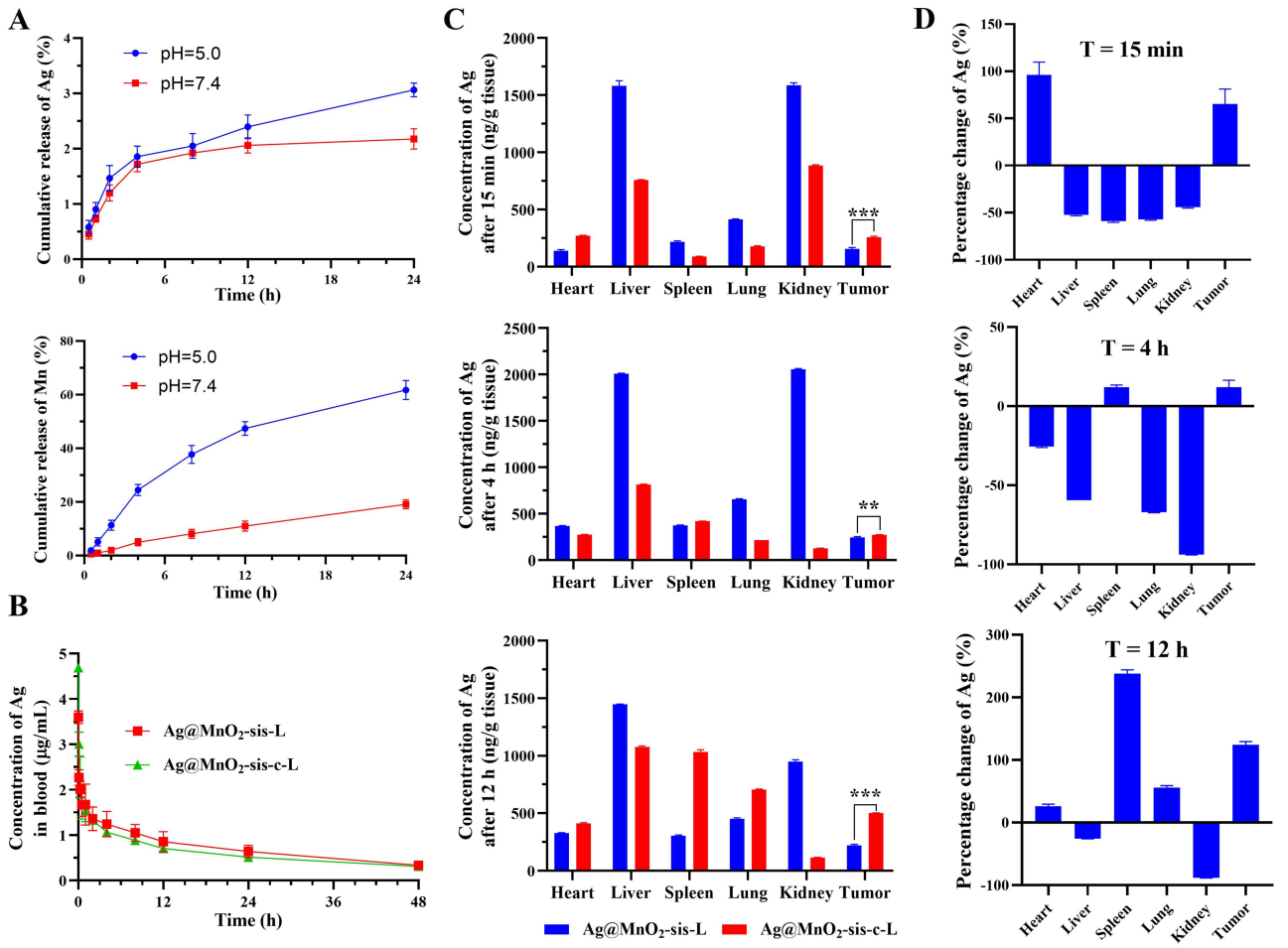

Figure 3 (**A**) Release of Ag and Mn from Ag@MnO_2-sis-c-L at different time-points; (**B**) Ag concentration-time curves of the preparations in blood (n=3); (**C**) The tissue distribution of Ag at time points (n=3); (**D**) The rates of change in relative Ag contents in tissues at time-points of 0.5 h (**A**), 4 h (**B**), and 12 h (**C**) (**P<0.01, ***P<0.001).

Biodistribution

The concentration of Ag in each sample in Ag@MnO_2-sis-c-L was normalized to that in Ag@MnO_2-sis-L, which served as the reference. As shown in Figure 3C and D, in normal tissues, at 15 min, the percentage of Ag content in the heart tissue of Ag@MnO_2-sis-c-L nanoparticles was higher than that of Ag@MnO_2-sis-L nanoparticles; however, there is no significant difference in the absolute concentration. In Figure 3C, the nanoparticles show noticeable accumulation in the kidney within 15 minutes. While clearance occurs over time, it is more gradual compared to the non-targeted formulation, indicating sustained presence and potential for prolonged therapeutic effects. At 4 h, the Ag content in the spleen tissue increased slightly, whereas it decreased in other tissues except for the tumor tissue. At 12 h, Ag content in the heart and lung tissues increased slightly, and there was a significant increase in the spleen. The nanoparticles did not end up in major organs but were mainly on the target side. The one exception is the spleen: nanoparticles often accumulate in the spleen due to their unique role in filtering blood and immune surveillance. The spleen contains specialized macrophages and dendritic cells in the marginal zone (MZ) and red pulp that efficiently capture nanoparticles, especially those larger than 100–200 nm. These particles are unable to cross the endothelial slits in the splenic sinuses and are thus retained and processed by splenic macrophages. Additionally, the composition and surface properties of nanoparticles, such as the presence of anionic or cationic lipids, influence their uptake by specific splenic cells.[37,38] The findings of this study suggest that, based on their accumulation profile, these nanoparticles may also exhibit therapeutic potential for lung-related cancers. Although nanoparticle accumulation in the spleen is often considered a drawback due to concerns about potential toxicity and reduced availability at target sites, our study demonstrates that despite visible spleen accumulation,

https://doi.org/10.2147/IJN.S510514

there are no signs of tissue toxicity (H&E staining results (Figure S1). These findings serve as proof of concept, confirming the feasibility of this nanoparticle system. Furthermore, the formulation can be further optimized to enhance therapeutic benefits by improving targeted delivery while maintaining a favorable safety profile. Additionally, the concentration of Ag@MnO_2-sis-L in tumor tissue increased steadily over the first 4 hours before starting to decline. In contrast, Ag@MnO_2-sis-c-L accumulated in the tumor for up to 12 hours at a significantly higher rate than Ag@MnO_2 -sis-L. The distribution characteristics of Ag@MnO_2-sis-c-L may be attributed to the combined action of passive and active transport, which are the enhanced permeability and retention (EPR) effect[39] and cRGD-mediated tumor targeting and internalization.[40]

Anti-Tumor Efficacy

Analysis of the tumor weight and volume change curves showed that the tumor weight and growth curves of mice in the Free sis group were not significantly different from those of the model group (P>0.05), indicating a poor inhibitory effect on tumor growth (Figure 4A and B). In contrast, a significant difference in tumor weight was evident between the siRNA groups (Ag@MnO_2-sis-c-L and Ag@MnO_2-scrsis-c-L) and the model group (P<0.05). Furthermore, tumor weights of the light-exposed groups were markedly reduced compared with those of the formulation and model groups that were not exposed to light (P<0.05). Additionally, the Ag@MnO_2-sis-c-L-NIR group exhibited a smaller tumor volume than the Ag@MnO_2-c-L-NIR group. This could be attributed to the fact that PTT leads to an increase in the survivin protein in the tumor area,[41] which is known to promote the proliferation of tumor cells. When sis was incorporated into the

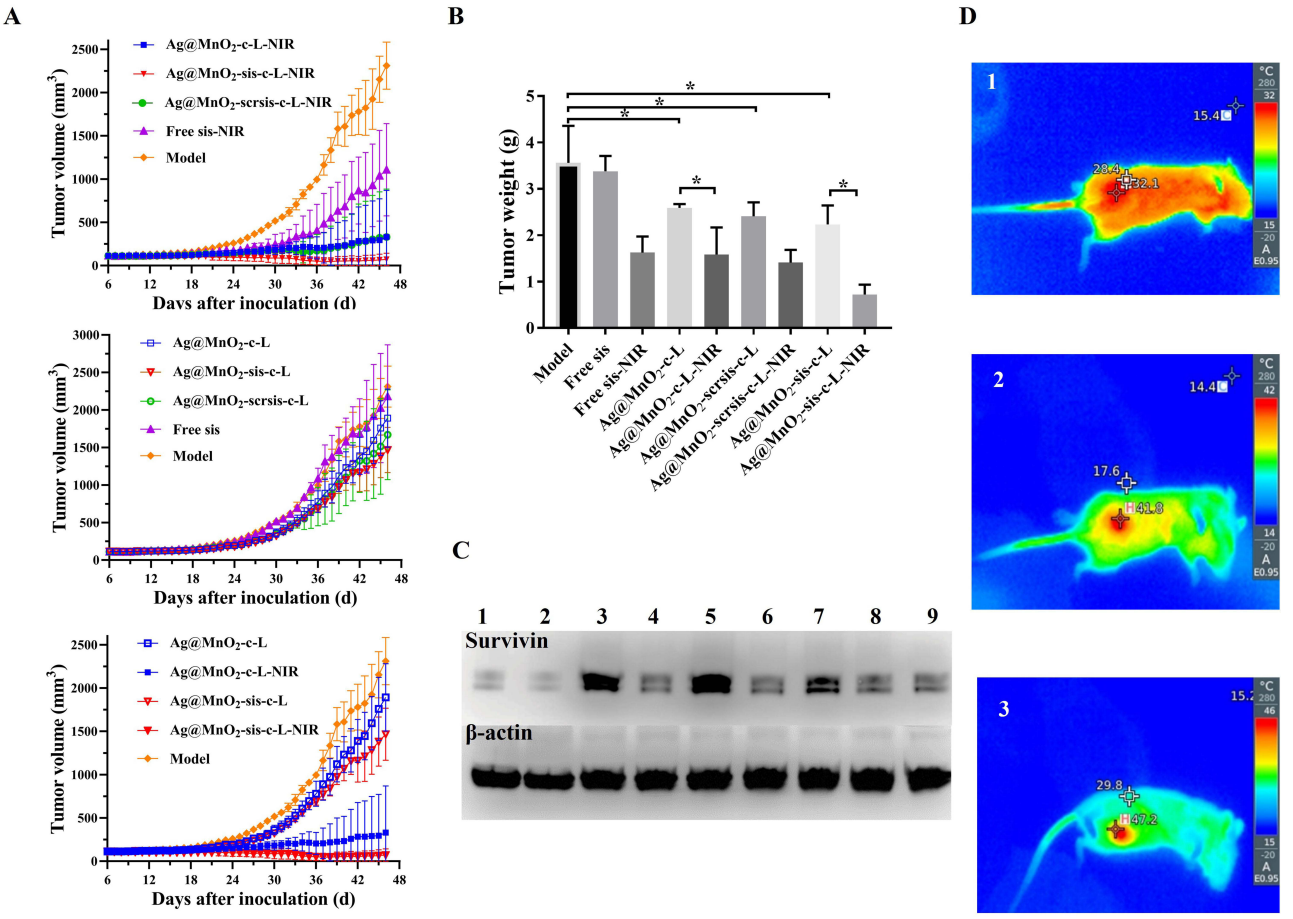

Figure 4 (**A**) Tumor volumes of mice from each preparation-treated group (n=3); (**B**) Tumor weights of mice in each group (*P<0.05); (**C**) Survivin and β-actin protein expression in tumor tissues of each group (1: Ag@MnO_2-sis-c-L-NIR, 2: Ag@MnO_2-sis-c-L, 3: Ag@MnO_2-scrsis-c-L-NIR, 4: Ag@MnO_2-scrsis-c-L, 5: Ag@MnO_2-c-L-NIR, 6: Ag@MnO_2-c-L, 7: Free sis-NIR, 8: Free sis, 9: Model); (**D**) Thermography of mice from the model group (1), low-dose (2) and high-dose (3) of Ag@MnO_2-sis -c-L-treatment groups (Ag equivalents of 37.5 μg/mL and 75.0 μg/mL, respectively).

nanoparticles, a better anti-tumor therapeutic effect was observed, indicating that the nanoparticles successfully delivered sis to the targeted site and effectively silenced the survivin protein production process, which was triggered by PTT treatment. In particular, the Ag@MnO_2-sis-c-L-NIR group displayed the lowest tumor weight and a nearly flat tumor growth curve, clearly indicating a trend of tumor growth inhibition. These results are consistent with the tissue distribution results (Figure 3C and D) and indicate that PTT with gene therapy possesses a synergistic therapeutic effect.

Western Blot

The formulations containing scrambled siRNA (scrsis) and those without the siRNA exerted no effects on the expression of survivin protein under non-illuminated conditions, however, upon light exposure, increased tissue expression of survivin protein was observed which can increase the survival rate of cancer cells,[20,42] as shown in Figure 4C. Both Ag@MnO_2-sis-c-L-NIR and Ag@MnO_2-sis-c-L suppressed the target protein expression and effectively counteracted the increase in survivin protein levels under light exposure. This finding was consistent with the strongest anti-tumor efficacy recorded for Ag@MnO_2-sis-c-L-NIR.

In vivo Photothermal Conversion Experiments

In mice in the model group, the temperature of the tumor area was 32.8°C, which was only slightly different from the surrounding skin temperature (Figure 4D). In contrast, following administration of Ag@MnO_2-sis-c-L at low dose of Ag equivalents of 37.5 μg/mL, the temperature in the tumor area of mice reached 41.8°C and further increased to 47.2°C at a high dose of Ag@MnO_2-sis-c-L (Ag equivalents of 75.0 μg/mL), indicating a significant temperature difference. Additionally, Figure 4D shows that the temperature of the irradiated area was significantly higher than that of the non-irradiated area, which indicates that PTT can effectively concentrate light energy on the lesion site with minimal harm to normal tissues.[32] Overall, compared to the model group, Ag@MnO_2-sis-c-L demonstrated strong photothermal conversion capability within the body, rapidly reaching 47.2°C under infrared laser irradiation, thereby leveraging the photothermal therapeutic effect of metal nanoparticles.

MRI Scanning

MRI signal intensity (commonly visualized as brightness) reflects the spatial distribution and relaxation properties of contrast agents. MnO_2 in Ag@MnO_2-sis-c-L nanoparticles acts as a contrast agent due to Mn^{2+} ions after degradation of the MnO_2 core for T_1-weighted magnetic resonance (MR) imaging, which shortens proton longitudinal relaxation times (T1) and enhances signal brightness.[43] As shown in Figure 5A, the whole-body imaging at 0.167 and 0.5 h post-injection exhibited significantly increased signal intensity compared to later time points, indicating rapid nanoparticle distribution and initial tumor accumulation. Notably, from 0.5 to 3 h, tumor-specific brightness persisted while systemic signals diminished, demonstrating remarkable tumor-selective retention. This suggests the nanoparticles' enhanced permeability and retention (EPR) effect in the tumor microenvironment, combined with potential active targeting mediated by the cRGD ligand modification. The MRI results demonstrated the contrast capability of the nanoparticles, which could be effectively employed in theranostic applications.

Monitoring of Mouse Weights

As illustrated in Figure 5B, the body weights of mice in all treatment groups fluctuated within a certain range, but maintained an overall stable trend, indicating that the formulation was effective in treating tumors while preserving the health and vitality of the experimental animals, resulting in no appreciable weight loss. The toxicological effects of AgNPs include oxidative stress, mitochondrial dysfunction, and metabolic disruptions, which can indirectly influence weight by altering metabolic or physiological processes.[44,45]

Biochemical Parameter Determination

In addition to the treatment effects on tumors and no significant toxicity of the nanodrug formulations, we observed no significant changes in the levels of biochemical indicators (including AST, ALT, BUN, and CRE-L) in the treatment groups relative to the model group, confirming the absence of damage to the normal liver and kidney functions (Table 3).

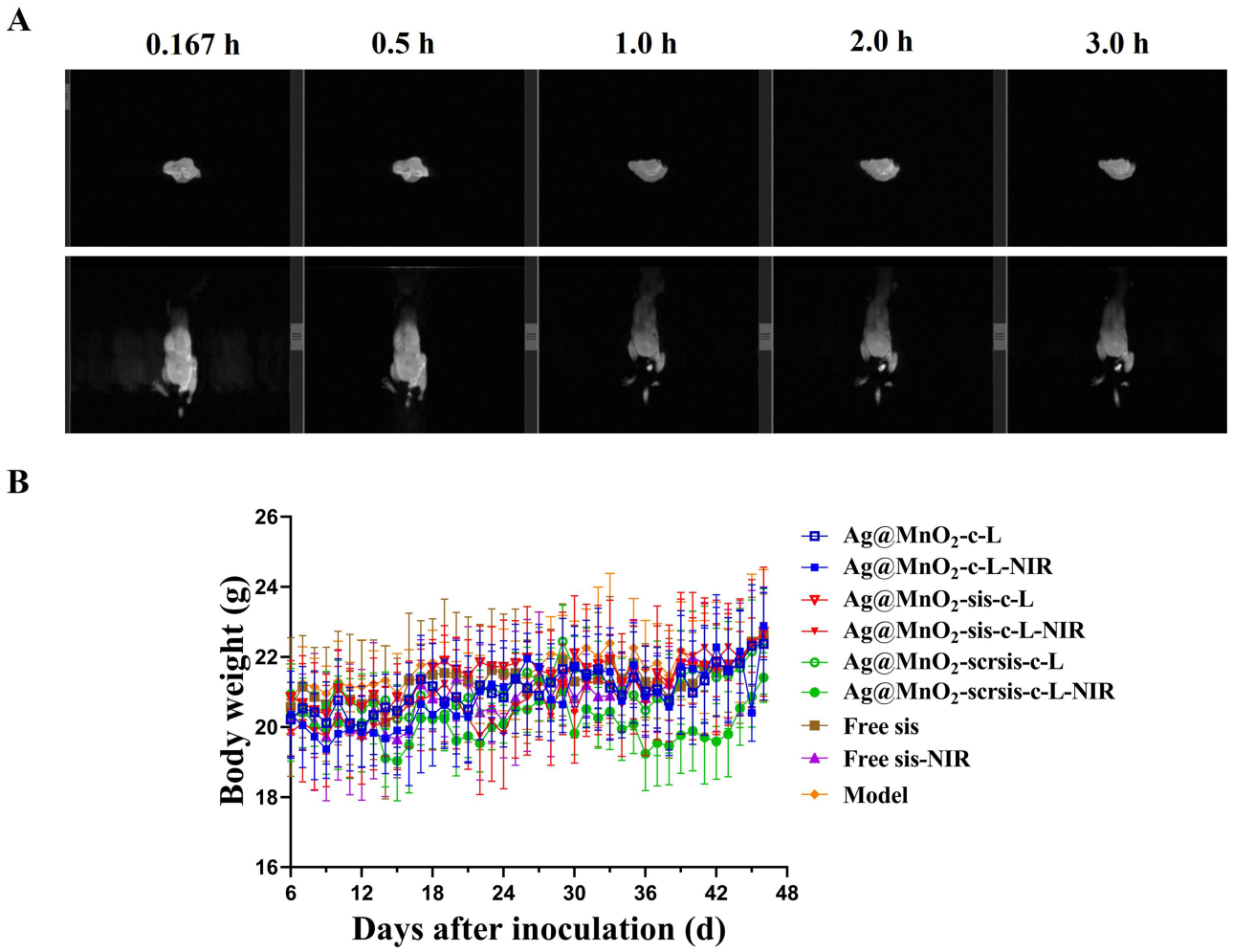

Figure 5 (**A**) MRI images of Ag@MnO_2-sis-c-L in mice at different time points (horizontal plane in the upper line, coronal plane in the lower line); (**B**) Changes in body weights of mice from each treatment group (n=3).

The results are consistent with those of H&E staining (Figure S1). In the anti-tumor experiments, observations of mouse weight, biochemical indicators, and HE staining results revealed that Ag@MnO_2-sis-c-L nanoparticles have relatively low systemic toxicity, which corresponds with the biodistribution results. The tumor-targeting characteristics of the Ag@MnO_2-sis-c-L nanoparticles and their distribution in smaller quantities in the major organs except for the spleen, could be credited.

Table 3 Biochemical Parameters of Mice in Each Group (n=3)

Formulation	ALT(U/L)	AST(U/L)	AST/ALT	BUN (μmol/L)	CRE-L(mmol/l)
Ag@MnO_2-c-L	258 ± 3.39	30 ± 1.56	9 ± 0.33	12 ± 2.69	14 ± 2.40
Ag@MnO_2-c-L-NIR	269.5 ± 43.13	56.5 ± 9.19	11 ± 2.38	7 ± 2.05	9 ± 0.21
Ag@MnO_2-sis-c-L	375 ± 1.48	46 ± 2.05	8 ± 0.40	7 ± 0.04	13 ± 4.31
Ag@MnO_2-sis-c-L-NIR	211.5 ± 0.71	43 ± 7.07	5 ± 1.23	7 ± 1.63	10 ± 1.84
Ag@MnO_2-scrsis-c-L	341 ± 8.27	30 ± 1.56	11 ± 0.31	7 ± 1.48	11 ± 0.28
Ag@MnO_2-scrsis-c-L-NIR	187 ± 15.56	40 ± 7.07	5 ± 1.23	7 ± 1.63	10 ± 1.84
Free sis	264 ± 42.92	38 ± 8.56	7 ± 2.77	8 ± 0.71	12 ± 0.28
Free sis-NIR	316 ± 4.95	30 ± 7.07	11 ± 2.38	7 ± 2.05	9 ± 0.21
Model	234 ± 3.32	38 ± 7.78	6 ± 1.23	9 ± 1.41	11 ± 0.07

Abbreviations: ALT, alanine aminotransferase; AST, aspartate aminotransferase; BUN, blood urea nitrogen; CRE-L, creatinine.

Conclusion

Ag@MnO_2-sis-c-L nanoparticles have several beneficial characteristics, including small particle size and PDI, sustained release, good sis loading capability, long-term effects in serum, and good photothermal conversion ability. In vivo, Ag@MnO_2-sis-c-L nanoparticles significantly reduced the tumor volume and expression of survivin at tumor locations, with good tumor-targeted imaging capability and no significant toxicity. Overall, the targeted Ag@MnO_2-sis -c-L nanoparticles have favorable physical and chemical properties, as well as significant anti-tumor efficacy in vivo and are therefore expected to achieve integrated photothermal diagnostic and therapeutic applications.

Acknowledgments

We greatly acknowledge the financial support of the National Natural Science Foundation of China (No. 82260695), Jiangxi Provincial Natural Science Foundation (20232ACB206062), Research Project of Jiangxi Provincial Department of Education (GJJ2400823), Jiangxi Provincial Administration of Traditional Chinese Medicine (TCM) Science and Technology Program (2024B0160), Innovation Team and Talents Cultivation Program of National Administration of Traditional Chinese Medicine (ZYYCXTD-D-202207), Young Jinggang Scholar of Jiangxi Province (J.Z.), New Century Talents Project of Jiangxi Province (2017082, X.L. and 2020028, J.Z.), Jiangxi University of Chinese Medicine Science and Technology Innovation Team Development Program (CXTD22001, CXTD22006), Jiangxi University of Chinese Medicine 1050 Youth Talent Project (X.L.), Jiangxi University of Traditional Chinese Medicine Special Zone Construction Project of Traditional Chinese Medicine (New Drug Creation Direction) (TQ-20; TQ-33) and College Students' Innovation and Entrepreneurship Training Program of Jiangxi Province and Jiangxi University of Chinese Medicine.

Author contributions

All authors made a significant contribution to the work reported, whether that is in the conception, study design, execution, acquisition of data, analysis and interpretation, or in all these areas; took part in drafting, revising or critically reviewing the article; gave final approval of the version to be published; have agreed on the journal to which the article has been submitted; and agree to be accountable for all aspects of the work.

Disclosure

The authors report no conflicts of interest in this work.

References

1. Lei S, Zheng R, Zhang S, et al. Global patterns of breast cancer incidence and mortality: a population-based cancer registry data analysis from 2000 to 2020. *Cancer Commun*. 2021;41(11):1183–1194. doi:10.1002/cac2.12207
2. Hou X, Chen Q, Fang Y, et al. iRGD-guided silica/gold nanoparticles for efficient tumor-targeting and enhancing antitumor efficacy against breast cancer. *Int J Nanomedicine*. 2024;19:8237–8251. doi:10.2147/ijn.S474135
3. Bray F, Ferlay J, Soerjomataram I, Siegel RL, Torre LA, Jemal A. Global cancer statistics 2018: GLOBOCAN estimates of incidence and mortality worldwide for 36 cancers in 185 countries. *CA*. 2018;68(6):394–424. doi:10.3322/caac.21492
4. Sung H, Ferlay J, Siegel RL, et al. Global cancer statistics 2020: GLOBOCAN estimates of incidence and mortality worldwide for 36 cancers in 185 countries. *CA*. 2021;71(3):209–249. doi:10.3322/caac.21660
5. Slamon DJ, Leyland-Jones B, Shak S, et al. Use of chemotherapy plus a monoclonal antibody against HER2 for metastatic breast cancer that overexpresses HER2. *N Engl J Med*. 2001;344(11):783–792. doi:10.1056/nejm200103153441101
6. Sun J, Zhao H, Xu W, Jiang GQ. Recent advances in photothermal therapy-based multifunctional nanoplatforms for breast cancer. *Front Chem*. 2022;10:1024177. doi:10.3389/fchem.2022.1024177
7. Zhao L, Zhang X, Wang X, Guan X, Zhang W, Ma J. Recent advances in selective photothermal therapy of tumor. *J Nanobiotech*. 2021;19(1):335. doi:10.1186/s12951-021-01080-3
8. Zhong YT, Cen Y, Xu L, Li SY, Cheng H. Recent progress in carrier-free nanomedicine for tumor phototherapy. *Adv Healthcare Mater*. 2023;12(4): e2202307. doi:10.1002/adhm.202202307
9. Wang J, Zhao S, Chen J, et al. Phage-Ce6-manganese dioxide nanocomposite-mediated photodynamic, photothermal, and chemodynamic therapies to eliminate biofilms and improve wound healing. *ACS Appl Mater Interfaces*. 2023;15(18):21904–21916. doi:10.1021/acsami.3c01762
10. Chen Q, Feng L, Liu J, et al. Intelligent albumin-MnO2 nanoparticles as pH-/H2 O2 -responsive dissociable nanocarriers to modulate tumor hypoxia for effective combination therapy. *Adv Mater*. 2016;28(33):7129–7136. doi:10.1002/adma.201601902
11. Lopes SV, Walczak P, Janowski M, Reis RL, Silva-Correia J, Oliveira JM. Cytocompatible manganese dioxide-based hydrogel nanoreactors for MRI imaging. *Biomater Adv*. 2022;134:112575. doi:10.1016/j.msec.2021.112575

12. Wu M, Hou P, Dong L, et al. Manganese dioxide nanosheets: from preparation to biomedical applications. *Int J Nanomedicine*. 2019;14:4781–4800. doi:10.2147/ijn.S207666
13. Zhang J, Wang F, Yalamarty SSK, Filipczak N, Jin Y, Li X. Nano silver-induced toxicity and associated mechanisms. *Int J Nanomedicine*. 2022;17:1851–1864. doi:10.2147/ijn.S355131
14. Pan Q, Zhang J, Li X, et al. Construction of novel multifunctional luminescent nanoparticles based on DNA bridging and their inhibitory effect on tumor growth. *RSC Adv*. 2019;9(26):15042–15052. doi:10.1039/c9ra01381d
15. De Matteis V. Exposure to inorganic nanoparticles: routes of entry, immune response, biodistribution and in vitro/in vivo toxicity evaluation. *Toxics*. 2017;5(4):29. doi:10.3390/toxics5040029
16. Bansod SD, Bawaskar MS, Gade AK, Rai MK. Development of shampoo, soap and ointment formulated by green synthesised silver nanoparticles functionalised with antimicrobial plants oils in veterinary dermatology: treatment and prevention strategies. *IET nanobiotech*. 2015;9(4):165–171. doi:10.1049/iet-nbt.2014.0042
17. Katifelis H, Lyberopoulou A, Mukha I, et al. Ag/Au bimetallic nanoparticles induce apoptosis in human cancer cell lines via P53, CASPASE-3 and BAX/BCL-2 pathways. *Artif Cells Nanomed Biotechnol*. 2018:46(sup3):S389–s398. doi:10.1080/21691401.2018.1495645
18. Velgosova O, Mačák L, Múdra E, Vojtko M, Lisnichuk M. Preparation, structure, and properties of PVA-AgNPs nanocomposites. *Polymers*. 2023;15(2):379. doi:10.3390/polym15020379
19. Hongxia L. Expression and pathological significance of Survivin and Ezrin proteins in breast cancer tissue. *Chin J Gerontol*. 2021;23(41):5387–5389.
20. Ferrario A, Gomer CJ. Targeting the 90 kDa heat shock protein improves photodynamic therapy. *Cancer Lett*. 2010;289(2):188–194. doi:10.1016/j.canlet.2009.08.015
21. Alshaer W, Zureigat H, Al Karaki A, et al. siRNA: mechanism of action, challenges, and therapeutic approaches. *Eur J Pharmacol*. 2021;905:174178. doi:10.1016/j.ejphar.2021.174178
22. Gajbhiye KR, Gajbhiye V, Siddiqui IA, Gajbhiye JM. cRGD functionalised nanocarriers for targeted delivery of bioactives. *J Drug Target*. 2019;27(2):111–124. doi:10.1080/1061186x.2018.1473409
23. Pan J, Attia SA, Subhan MA, et al. Monoclonal antibody 2C5-modified mixed dendrimer micelles for tumor-targeted codelivery of chemotherapeutics and siRNA. *Mol Pharm*. 2020;17(5):1638–1647. doi:10.1021/acs.molpharmaceut.0c00075
24. Gopiraman M, Bang H, Yuan G, et al. Noble metal/functionalized cellulose nanofiber composites for catalytic applications. *Carbohydr Polym*. 2015;132:554–564. doi:10.1016/j.carbpol.2015.06.051
25. Lei M, Gao M, Yang X, et al. Size-controlled au nanoparticles incorporating mesoporous zno for sensitive ethanol sensing. *ACS Appl Mater Interfaces*. 2021;13(44):51933–51944. doi:10.1021/acsami.1c07322
26. Nakayama M, Tagashira H. Electrodeposition of layered manganese oxide nanocomposites intercalated with strong and weak polyelectrolytes. *Langmuir*. 2006;22(8):3864–3869. doi:10.1021/la053072i
27. Ferraresso F, Strilchuk AW, Juang LJ, Poole LG, Luyendyk JP, Kastrup CJ. Comparison of DLin-MC3-DMA and ALC-0315 for siRNA delivery to hepatocytes and hepatic stellate cells. *Mol Pharm*. 2022;19(7):2175–2182. doi:10.1021/acs.molpharmaceut.2c00033
28. Tian MP, Song RX, Wang T, Sun MJ, Liu Y, Chen XG. Inducing sustained release and improving oral bioavailability of curcumin via chitosan derivatives-coated liposomes. *Int J Biol Macromol*. 2018;120(Pt A):702–710. doi:10.1016/j.ijbiomac.2018.08.146
29. Chen J, Rizvi A, Patterson JP, Hawker CJ. Discrete libraries of amphiphilic poly(ethylene glycol) graft copolymers: synthesis, assembly, and bioactivity. *J Am Chem Soc*. 2022;144(42):19466–19474. doi:10.1021/jacs.2c07859
30. Gregersen CH, Mearraoui R, Søgaard PP, et al. Lipid nanoparticles containing labile PEG-lipids transfect primary human skin cells more efficiently in the presence of apoE. *Eur J Pharm Biopharm*. 2024;197:114219. doi:10.1016/j.ejpb.2024.114219
31. Zhang Y, Li S, Zhou X, et al. Construction of a targeting nanoparticle of 3',3″-Bis-Peptide-siRNA conjugate/mixed lipid with postinserted DSPE-PEG2000-cRGD. *Mol Pharm*. 2019;16(12):4920–4928. doi:10.1021/acs.molpharmaceut.9b00800
32. Overchuk M, Weersink RA, Wilson BC, Zheng G. Photodynamic and photothermal therapies: synergy opportunities for nanomedicine. *ACS Nano*. 2023;17(9):7979–8003. doi:10.1021/acsnano.3c00891
33. Hopkins E, Sanvictores T, Sharma S. Physiology, acid base balance. *StatPearls*. 2024.
34. Taghipour YD, Zarebkohan A, Salehi R, et al. Enhanced docetaxel therapeutic effect using dual targeted SRL-2 and TA1 aptamer conjugated micelles in inhibition Balb/c mice breast cancer model. *Sci Rep*. 2024;14(1):24603. doi:10.1038/s41598-024-75042-8
35. Subhan MA, Parveen F, Filipczak N, Yalamarty SSK, Torchilin VP. Approaches to improve EPR-based drug delivery for cancer therapy and diagnosis. *J Pers Med*. 2023;13(3):389. doi:10.3390/jpm13030389
36. Pannuzzo M, Esposito S, Wu LP, et al. Overcoming nanoparticle-mediated complement activation by surface PEG pairing. *Nano Lett*. 2020;20(6):4312–4321. doi:10.1021/acs.nanolett.0c01011
37. Cataldi M, Vigliotti C, Mosca T, Cammarota M, Capone D. Emerging role of the spleen in the pharmacokinetics of monoclonal antibodies, nanoparticles and exosomes. *Int J Mol Sci*. 2017;18(6):1249. doi:10.3390/ijms18061249
38. Li J, Wang H. Selective organ targeting nanoparticles: from design to clinical translation. *Nanoscale Horiz*. 2023;8(9):1155–1173. doi:10.1039/d3nh00145h
39. Wu J. The Enhanced Permeability and Retention (EPR) effect: the significance of the concept and methods to enhance its application. *J Pers Med*. 2021;11(8):771. doi:10.3390/jpm11080771
40. Yan W, Guo B, Wang Z, Yang J, Zhong Z, Meng F. RGD-directed 24 nm micellar docetaxel enables elevated tumor-liver ratio, deep tumor penetration and potent suppression of solid tumors. *J Control Release*. 2023;360:304–315. doi:10.1016/j.jconrel.2023.06.032
41. Wen Z, Liu F, Liu G, et al. Assembly of multifunction dyes and heat shock protein 90 inhibitor coupled to bovine serum albumin in nanoparticles for multimodal photodynamic/photothermal/chemo-therapy. *J Colloid Interface Sci*. 2021;590:290–300. doi:10.1016/j.jcis.2021.01.052
42. Siragusa G, Tomasello L, Giordano C, Pizzolanti G. Survivin (BIRC5): implications in cancer therapy. *Life Sci*. 2024;350:122788. doi:10.1016/j.lfs.2024.122788
43. Xie M, Duan T, Wan Y, et al. Ultrasound and glutathione dual-responsive biomimetic nanoplatform for ultrasound/magnetic resonance imaging and sonodynamic therapy of ovarian cancer. *J Colloid Interface Sci*. 2025;682:311–323. doi:10.1016/j.jcis.2024.11.221
44. Jarak I, Carrola J, Barros AS, et al. From the cover: metabolism modulation in different organs by silver nanoparticles: an NMR metabolomics study of a mouse model. *Toxicol Sci*. 2017;159(2):422–435. doi:10.1093/toxsci/kfx142
45. Noga M, Milan J, Frydrych A, Jurowski K. Toxicological aspects, safety assessment, and green toxicology of silver nanoparticles (AgNPs)—critical review: state of the art. *Int J Mol Sci*. 2023;24(6):5133. doi:10.3390/ijms24065133